Date of publication xxxx 00, 0000, date of current version xxxx 00, 0000.

Digital Object Identifier 10.1109/ACCESS.2017.Doi Number

A Multifunctional Single-phase EV On-board Charger with a New V2V Charging Assistance Capability

Seyedfoad Taghizadeh[1], Member, IEEE; M. J. Hossain[2], Senior Member, IEEE: Noushin Poursafar[1], Student Member, IEEE; Junwei Lu[3], Senior Member, IEEE; and Georgios Konstantinou[4], Senior Member, IEEE

[1]School of Engineering, Macquarie University, 2109 NSW, Australia
[2]School of Electrical and Data Engineering, University of Technology Sydney, 2007 NSW, Australia
[3]Department of Science and Engineering, Griffith University, 4111 QLD, Australia
[4]School of Electrical Engineering and Telecommunications, University of New South Wales, 2052 NSW, Australia

Corresponding author: Seyedfoad Taghizadeh (e-mail: s.t.taghizadeh@ieee.org).

ABSTRACT This paper presents the design and implementation of a single-phase multifunctional electric-vehicle (EV) on-board charger with an advanced vehicle-to-vehicle (V2V) functionality for emergency roadside charging assistance situations. Using this function, an EV is able to charge from another EV in case of an emergency when the battery is flat and there is no access to a charging station. The designed EV charger can support the proposed V2V function with rated power and without the need for an additional portable charger. It can also provide conventional main and ancillary functions such as vehicle-to-grid (V2G), grid-to-vehicle (G2V), reactive power support, harmonics reduction and grid-voltage regulation. All the functions are addressed in the control part through the sharing of existing converters in an all-in-one system. The proposed EV charger is designed and simulated in MATLAB/Simulink, and a laboratory prototype is also implemented to validate its key functions.

INDEX TERMS Vehicle to vehicle (V2V), grid to vehicle (G2V), vehicle to grid (V2G), static synchronous compensator (STATCOM), active power filter (APF).

I. INTRODUCTION

The number of plug-in electric vehicles (EVs) is growing rapidly in developed countries and, accordingly, they have drawn widespread attention due to their various potential functions on the grid. Conventionally, EVs are charged from the grid (G2V), possibly through single-phase or three-phase chargers. They can also operate as back-up energy units for the grid (V2G). Accordingly, EVs can discharge during peak hours when the total energy demand is high.

G2V and V2G, the main functions of EV chargers, are supported by bidirectional power electronic converters as the key components of EV chargers [1, 2]. Moreover, these converters can be utilized to provide ancillary functions for the grid, such as reactive power support, voltage regulation and/or harmonics reduction, which are conventionally provided by static synchronous compensators (STATCOMs) and/or active power filters (APFs). For example, an EV charger is designed to supply the reactive power demanded by non-linear loads while it charges or discharges an EV`s battery [3-6]. In another design, an EV charger works as an active power filter to reduce the harmonics of the grid-side current in a household network [7-9]. A single-phase EV charger is also able to regulate the voltage at the point of common coupling (PCC) by circulating leading or lagging VAR into the grid [10].

Recently, multifunctional EV chargers have been designed to support more than one ancillary function. A multifunctional EV charger in [11, 12] is able to support both reactive power and harmonics reduction while operating in G2V/V2G mode. In a later design, a single-phase EV charger is utilized to address the main functions as well as three ancillary functions (reactive power support, harmonics reduction and voltage regulation) simultaneously [13].

Single-phase EV chargers are also designed to support some functions in grid-isolated mode. Vehicle-to-home (V2H) operation is presented in [14, 15] for supporting linear electrical appliances in a house and then extended for supporting non-linear loads [11]. Accordingly, the EV operates as an uninterruptible power supply (UPS) that is off-line during the grid-connection mode and on-line during the grid-isolated mode. In another approach, the EV charger can

perform a traction-to-auxiliary (T2A) battery function. In [16] and [17], a non-isolated dc-dc converter is used between the traction and the auxiliary batteries so that, during the grid-isolated mode, the auxiliary battery can be charged from the traction battery. Nevertheless, this design does not follow the IEC 61851-1 standard, which mandates having galvanic isolation for the auxiliary battery [18]. The design is modified in [19, 20] by using an isolated unidirectional dc-dc converter, which enables the charging of the auxiliary battery from the traction battery while galvanic isolation is provided.

Nowadays, one of the main barriers to EV market growth is the insufficient number of charging stations. Even with significant progress in building charging stations in some countries, there is still a concern among many customers about an emergency situation in which their EV battery becomes unexpectedly flat and they do not have access to a charging station. Although such an emergency situation can also happen for existing fuel-based cars, the driver still has a chance to receive fuel from either roadside assistance or occasionally from another car. Such solutions need to be devised for EVs as well. If the EV owners have the opportunity to charge their cars from other EVs, which is called vehicle-to-vehicle (V2V) in this paper, their concerns about having a flat battery will be diminished significantly, paving the way for development of the EV market.

In recent years, a few aspects of V2V operation have been addressed in the literature, mostly about charging scheduling schemes for multiple EVs [21, 22] and charging strategies and energy management protocols for cooperative EV-to-EV charging [23-26] at a charging station. To address the problem of EVs becoming disabled because of an empty battery, roadside assistance trucks are proposed that use a huge master battery and a separate converter infrastructure to assist the disabled EV [27]. Although this solution is effective, there are still problems associated with cost, service fees, arrival times and availability.

As another interesting approach, a portable customer-used EV charging device is proposed in [28]. The portable charger, which is shown in Fig. 1(a), includes an internal dc-ac inverter and a set of connector cables to connect the dc battery terminals of the first vehicle, which has an internal combustion engine, to the ac charging port of the second vehicle, which is an EV. The portable device can enable V2V operation; however, this device is an extra off-board charging device that would need to be purchased by EV owners as a separate unit. Moreover, the V2V charging power is limited (up to 325 W) due to the circuit configuration of the portable charger and the limited output power of the first vehicle`s battery as reported in [28]. As a consequence, the design of an EV on-board charger that is able to address the V2V function without using extra charging infrastructure and a higher charging power ratio is not addressed.

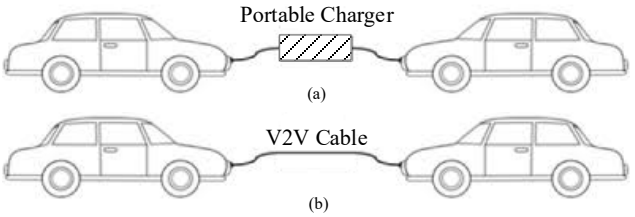

FIGURE 1. a) Conventional V2V operation, b) Proposed V2V operation.

This paper proposes a design for an EV on-board charger that is able to charge the EV via V2V operation. Using the proposed design, two EVs can be connected via a low-cost charging cable (referred to as a V2V cable in this paper) without the need for an additional portable charger (Fig. 1(b)). Moreover, the V2V operation can be accomplished with the maximum power ratio of the EV charger since the same charging infrastructure is used for transmitting the power between the EVs. The proposed V2V function is addressed in the control part, thus no additional converter needs to be added to the EV charger. Finally, to present a complete design, the proposed EV charger is also utilized to cover the conventional grid-connected functions such as G2V, V2G, reactive power support, harmonics reduction and voltage regulation for a household network.

The rest of the paper is organized as follows: Section II presents the proposed multifunctional EV charger. Section III shows the design considerations, mainly focusing on the proposed V2V function. The performance evaluation of the designed EV charger is presented in Section IV. This is followed by the conclusion of this research in Section V.

II. MULTIFUNCTIONAL EV CHARGER

Fig. 2 shows the proposed multifunctional EV on-board charger, which includes two converters. The back-end converter, which includes switches S_5, S_6 and inductor L on the battery side, has a single operational mode, operating as a bidirectional boost dc-dc converter during both the grid-connected and grid-isolated operational modes of the EV charger. The front-end H-bridge (HB1) shares the switches S_1, S_2, S_3, S_4 and inductors L_{f1}, L_{f2} for the two operational modes. This converter can be utilized to operate as either a dc-ac converter in V2V operation [Function I] or as a dc-ac converter during the grid-connected mode to provide G2V and V2G operation [Function II] as well as ancillary functions of STATCOM and/or APF [Functions III and IV].

A. Proposed V2V operation of the EV charger

The V2V operation between two EVs is shown in Fig. 2. During the V2V operation, the control system of HB1 in EVa is supposed to be rearranged from a grid-connected mode to V2V mode to set the amplitude and frequency of the ac voltage that is shared by the two EVs. As a result, HB1 in EVa operates with a different control strategy, and HB2 uses the same control algorithm to enable EVa to participate in the V2V operation.

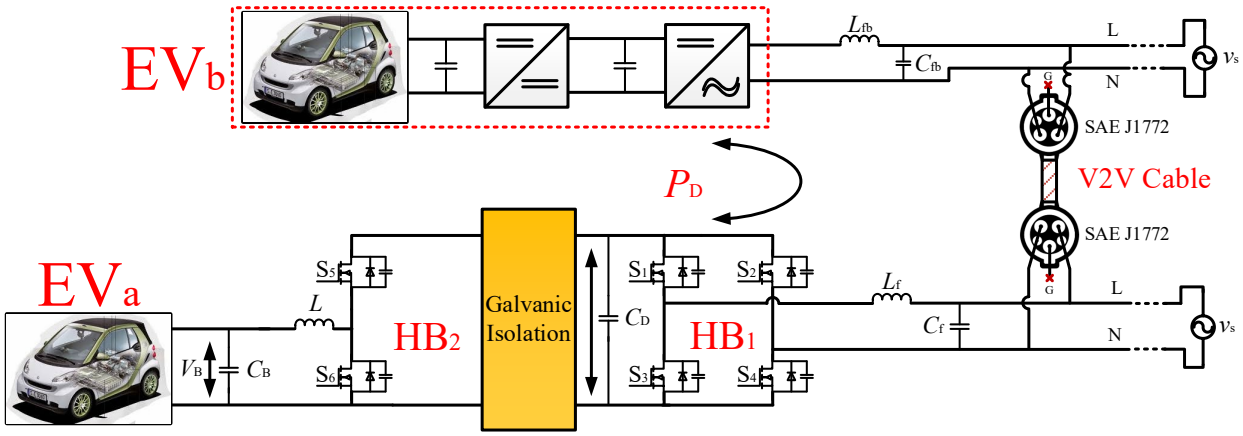

FIGURE 2. The multifunctional EV charger and its connection during V2V operation.

This rearrangement is accomplished using a V2V cable between the two connected EVs as shown in Fig. 2. On the other side, EVb uses the same control system of its grid-connected charging operation for its HB1 and HB2 to receive power from EVa. In other words, EVa acts as a new source of charge for EVb.

As shown in Fig. 2, a galvanic isolation can be placed between HB1 and HB2 via adding a dual-active-bridge (DAB) dc-dc converter controlled by a phase-shift controller [29]. Recently, galvanic isolation is required by some established standards to prevent current flow between the two stages of the charging system, thereby increasing safety and reliability. However, the DAB does not interfere with the proposed V2V operation since, as already explained, the V2V functionality is completely performed by changing the operational control mode of the front-end converter of EVa, HB1, while the other stages work with their previous operational mode. Accordingly, in this paper, the details of the design of the DAB and its control system are omitted and referred to [29].

The advantage of the proposed V2V approach is that the same components (switches, inductors and capacitors) are used for both the grid-connected mode and V2V operation. Furthermore, the V2V cable is interfaced between the existing charging ports of the two EVs. Therefore, no additional component and/or separate charging port is required for the V2V operation. This topology meets the mandatory standard SAE J1772, a North American standard for electrical connectors for EVs. As a result, the EV owners' safety during the V2V operation will be ensured. The only additional structure is the V2V cable. This includes two SAE J1772 sockets and an interface cable, which has a simple structure and can be manufactured at the same price as a normal charging cable.

The designed EV charger in this paper uses the most basic and common converter topology (H-bridge), which is used in most existing EV chargers [1, 30]. In the case of different topologies, only the control algorithms may need to be updated, which is supposed to be devised by the car manufacturers. It should be noted that the front-end converter (HB1), regardless of its topology, requires the L and N ports (and G port for grounding) to be connected to the grid. In addition, all the EV chargers are obliged to use the standard SAE J1772 sockets. Therefore, the structure of the V2V connection using the V2V cable will be similar for EV chargers with different converter topologies.

At present, there are some EV chargers on the market with a unidirectional front-end converter (HB1 in this paper). The proposed V2V operation requires the EV chargers to have bidirectional converters, and this seems to be a limitation for the proposed V2V operation in this paper. However, the EV chargers with a unidirectional structure are still able to participate in V2V operation while receiving charging assistance from another EV with a bidirectional charger. Moreover, the existing unidirectional EV chargers will almost certainly need to be replaced with bidirectional chargers in the future. The reason is that, in the near future, energy providers and utilities will demand to use the stored energy of the parked EVs as backup units for the power network, and if an EV charger has a unidirectional structure, it cannot deliver power into the grid, contradicting industrial demands. As a result, the manufacturing of unidirectional EV chargers will be discouraged by energy providers. Therefore, in this paper, the two EVs are assumed to be bidirectional.

III. DESIGN CONSIDERATION

In this section, the dynamic model and small-signal approximations of HB1 and HB2 in EVa are analytically presented and followed by presenting the design procedure of the proposed control systems during the V2V operation.

A. Modeling and control of an EV charger during V2V operation

Dynamic model and control of HB1: A cascaded control strategy, which is presented in [31], is used to regulate the front-end ac voltage v_s through controlling the ac current, i_c. As shown in Fig. 3, the control algorithm includes an inner current controller and outer voltage controller operating based on the DQ transformation technique. L_f, C_f, and ω are the inductance,

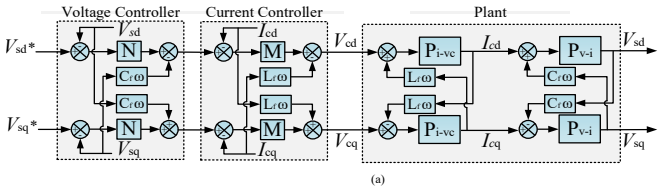

FIGURE 3. Block diagram of an HB1 control loop.

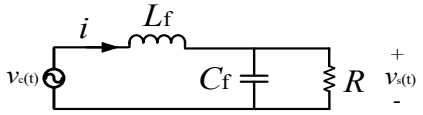

FIGURE 4. Equivalent circuit model of an LC filter.

the capacitance and the angular frequency of PWM, respectively. M and N represent the controllers of the current and voltage control loops, respectively. $P_{i-vc}(s)$ is the transfer function between the inductance current and the input voltage of the LC filter, and $P_{vs-i}(s)$ is the transfer function between the output voltage of the LC filter and the inductor current. Based on the equivalent circuit model presented in Fig. 4, $P_{i-vc}(s)$ and $P_{vs-i}(s)$ are given by

$$P_{i-vc}(s) = \frac{i(s)}{v_c(S)} = \frac{RC_f s + 1}{RL_f C_f s^2 + L_f s + R} \quad (1)$$

$$P_{vs-i}(s) = \frac{v_s(S)}{i(s)} = \frac{R}{RC_f s + 1} \quad (2)$$

Dynamic model and control of HB2: The control method presented in [32] is used for HB2. As shown in Fig. 5, a current controller $H(s)$ including a PI controller, is used to control the charging current, while its reference signal is generated by an outer voltage controller $C(s)$. In the outer voltage control loop, the dc-link voltage V_D is measured and compared with V_D^* (400 V in this paper), and a reference signal is generated for the inner current control loop.

Using the equivalent circuit model of the boost converter (Fig. 6) presented in [33], the transfer function of the output voltage is derived as follows:

$$\hat{v}(s) = \frac{D'}{LCs^2 + \frac{L}{R}s + D'^2}\hat{v}_B(s) + \frac{V}{D'}\frac{(-Ls + D'^2R)}{(RLCs^2 + Ls + RD'^2)}\hat{d}(s). \quad (3)$$

where V, I and D are the dc quiescent values of the dc-bus voltage, the inductor current and the duty cycle of the converter, respectively; and $\hat{v}$, $\hat{\imath}$ and $\hat{d}$ are their small ac variations. $\hat{v}_B$ is the small ac variation of the source voltage and $D' = 1 - D$. Accordingly, the transfer function between the duty cycle and the output voltage of the boost converter is given by

$$G_{vd}(s) = \frac{\hat{v}(s)}{\hat{d}(s)}\Big|_{\hat{v}_B(s)=0} = \frac{V}{D'}\frac{(-Ls + D'^2R)}{(RLCs^2 + Ls + RD'^2)}. \quad (4)$$

And the transfer function between the inductor current and the output voltage is expressed by

$$G_{vi}(s) = \frac{\hat{v}(s)}{\hat{\imath}(s)} = \frac{D'R}{RCs + 1}. \quad (5)$$

The transfer function between the duty cycle and the inductor current is

$$G_{id}(s) = \frac{\hat{\imath}(s)}{\hat{d}(s)} = \frac{G_{vd}(s)}{G_{vi}(s)} = \frac{V}{RD'^2}\frac{(-Ls + D'^2R)(RCs + 1)}{(RLCs^2 + Ls + RD'^2)}. \quad (6)$$

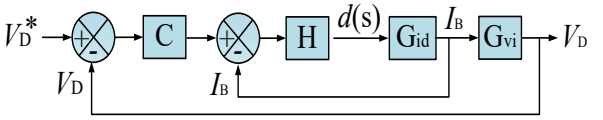

FIGURE 5. Block diagram of the double-control loop in a V2V operation.

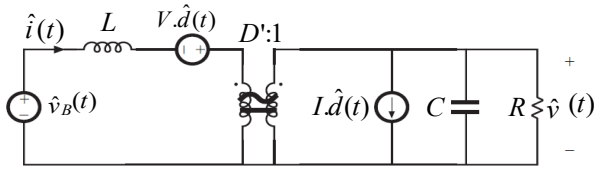

FIGURE 6. Equivalent circuit model of boost converter HB2.

TABLE I. System parameters

Symbol	Item	Quantity
v_s	Front-end voltage	220 V
V_D	DC-link voltage	400 V
f	Line frequency	50 Hz
f_{sw}	Switching frequency	50 kHz
L_f	Filter inductors	4 mH
C_f	Filter capacitor	1 mF
C_D	DC-link capacitor	1 mF
C_B	Battery-side capacitor	1 mF
L	DC-link inductor	4 mH

B. Design procedure

Based on the dynamic models in Section III-A and the parameters summarized in Table I, the control systems of HB1 and HB2 are designed in this section. Root locus analysis is used to design the controllers for HB1 and HB2.

Design of the current controller, M, for HB1: As already mentioned, a cascaded control algorithm including an outer voltage control loop and an inner current control loop (Fig. 3) is designed for HB1. To do so, first, the inner control loop needs to be designed. The plant, which is presented in (1), is used for the design, and K_{PM}/K_{IM} is set to 0.43, where K_{PM} and K_{IM} are the proportional gain and integral gain of the controller M, respectively. Since the EV charger is designed with a 4-kW power ratio, the rlocus of the current controller for a 4-kW load (or $R = 12\ \Omega$) is shown in Fig. 7. According to the trajectory of poles toward zeros and the damping factors, the optimum value of 350 is selected for K_{IM}. Because of the zero-pole cancellation, the closed loop response of the current controller is very fast and can be considered as unity for the rest of the analysis.

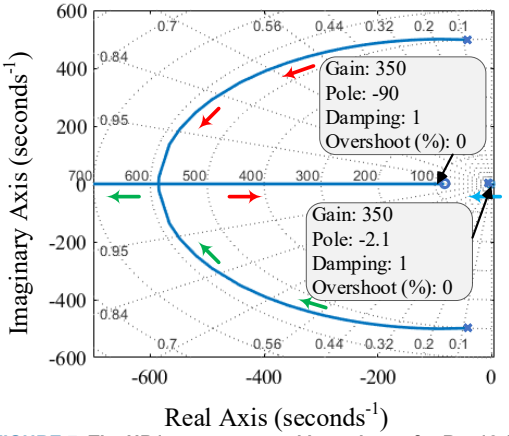

FIGURE 7. The HB1 current control loop rlocus for R = 12 Ω.

Design of the voltage controller, N, for HB1: A similar process is used to design the outer voltage controller, *N,* as shown in Fig. 3 for HB1. The rlocus of the voltage control loop for the load $R = 12\,\Omega$ is shown in Fig. 8, and K_{PN}/K_{IN} is selected as 0.1 where K_{PN} and K_{IN} are proportional and integral gains of N, respectively. Using the rlocus analysis, $K_{IN} = 5$ is selected to achieve a settling time of less than 0.3~s and a minimum overshoot (~ 0%).

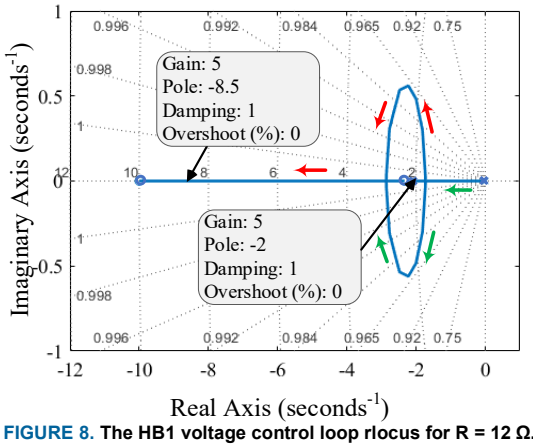

FIGURE 8. The HB1 voltage control loop rlocus for R = 12 Ω.

Design of the current controller, H, for HB2: The design process of the inner current controller, *H,* which is shown in Fig. 5, for HB2 is presented in this section. The transfer function of (6) is used, while the load is considered as $R = 40\,\Omega$ corresponding a 4-kW load. Figure 9 shows the rlocus of the current control loop via setting $K_{PH}/K_{IH} = 0.014$ where K_{PH} and K_{IH} are the proportional and integral gains of H, respectively. The design criterion in this paper is to find the fastest response with the lowest overshoot. Therefore, 0.4 is selected for K_{IH} to achieve a 0.3-s settling time and the minimum overshoot (~ 0%).

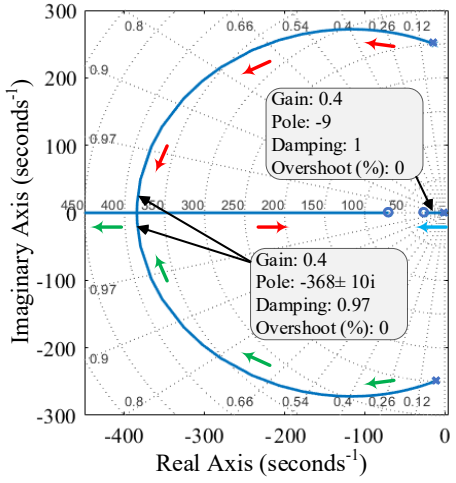

FIGURE 9. The HB2 current control loop rlocus for R = 40 Ω.

Design of the voltage controller, C, for HB2: To tune the outer voltage controller, which is shown in the LTI model in Fig. 5, the rlocus of the model is plotted (Fig. 10) for $R = 40\,\Omega$, and K_{PC}/K_{IC} is selected as 0.05 where K_{PC} and K_{IC} are the proportional and integral gain of C, respectively. The outcome of the design is to select $K_{IC} = 10$, which results in achieving the settling time of less than 0.3 s and 3% overshoot. Table II summarizes the designed control parameters for HB1 and HB2. These parameters are used for the rest of the analysis.

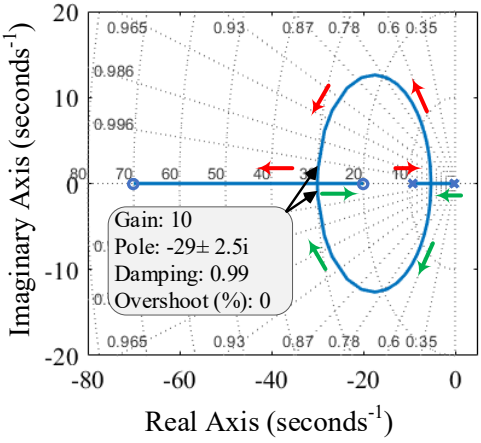

FIGURE 10. The HB2 voltage control loop rlocus for R = 40 Ω.

TABLE II. Control parameters

Controller	Controller Type	Control Parameters	
M	HB1 current controller	$K_{PM} = 150$	$K_{IM} = 350$
N	HB1 voltage controller	$K_{PN} = 0.5$	$K_{IN} = 5$
H	HB2 current controller	$K_{PH} = 0.005$	$K_{IH} = 0.4$
C	HB2 voltage controller	$K_{PC} = 0.5$	$K_{IC} = 10$

Fig. 11 shows the control block diagram of the designed EV charger during the V2V operation. In Fig. 11(a), the bus voltage V_D and the charging current I_B are regulated by HB2 using a bus-voltage controller and a battery-current controller, respectively. Meanwhile, HB1 with its control algorithm, which is shown in Fig. 11(b), regulates the amplitude and frequency of the front-end ac voltage v_s. As a result, HB1 operates in the constant-voltage charging mode.

The design of the proposed EV charger controller in the grid-connected mode has been presented in [13], and this section is omitted in this paper to avoid repetition. However, to make the paper self-explanatory, the control block diagram of the system in this mode is shown in Fig. 12.

Comparison of the control algorithms of Fig. 11 and Fig. 12 shows that HB2 has a similar control algorithm during both the V2V operation and the grid-connected mode, whereas HB1 uses two different control algorithms. It is concluded that switching the control algorithm of HB1 from V2V operation, as shown in Fig. 11, to the grid-connected mode, as shown in Fig. 12, (and vice versa) is required, which is explained in the following section.

C. Communication requirements

Switching from the grid-connected operational mode to V2V operation can be performed through communication and messaging between the two EV chargers. The communication between the EVs can be enabled through the V2V cable.

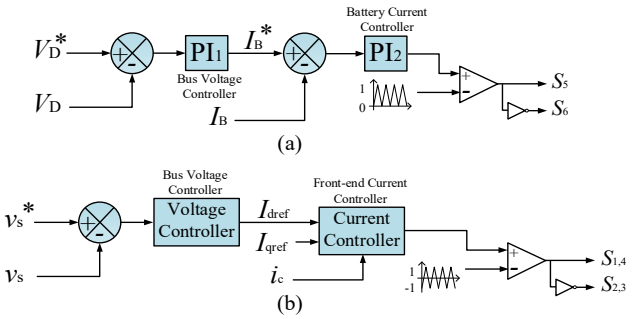

FIGURE 11. Control block diagrams of the EV charger during V2V operation: a) control algorithm of HB2, b) control algorithm of HB1.

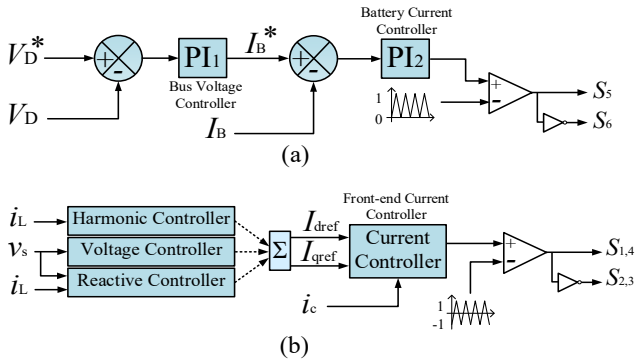

FIGURE 12. Control block diagrams of the EV charger during grid-connected mode [13]: a) control algorithm of HB2, b) control algorithm of HB1.

Figure 13 shows the SAE J1772 charging connector used to connect the V2V cable. According to the mandatory standard SAE J1772, this connector includes three power lines (L, N and G), a proximity detector that hinders the movement of the cars while they transmit the charging power, and a control pilot used for messaging between the chargers. During the V2V operation, a 12-V, 1-kHz signal is generated by each EV charger on the control pilot to detect the successful connection between the two EVs. When the V2V connection is detected and admitted by the EV chargers, the control system of the grid-connected operational mode (Fig. 12) is automatically switched to the control diagram of the V2V operation (Fig. 11). Thus, the V2V operation can be enabled. Using the proximity detection port and the control pilot, the V2V operation can be performed while the mandatory safety requirements are met. If the V2V connection is not successful, the power pins of the SAE J1772 have no voltage and no power to flow through the V2V cable. This ensures the safety of people. Optionally, the 1-kHz signal on the control pilot can also be used to adjust the V2V charging level. Such an interaction between the EV charger and the EV owner is addressed by the newly established standard SAE J2836/5. It should be noted that specifications such as physical communication infrastructure, communication methods and protocols are not within the scope of this paper and are targeted as future work.

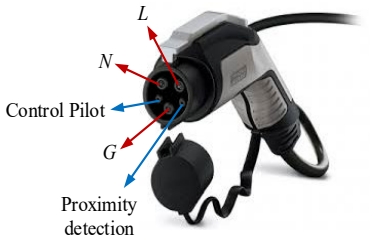

FIGURE 13. SAE J1772 charging connector of the V2V cable.

D. Protection requirements

During both the grid-connected and V2V operation, both front-end phase and neutral conductors are facilitated by hardware-based relays and software-based comparators. During a short-circuit event, the software-based comparators first sense the over-current incident and quickly block the gate signals to shut down the whole system. In case of any failure in software-based protection, which is unlikely to happen, the relays will disconnect the EV charger from the rest of the system. The same hardware-based and software-based over-current protection facilities are used at the battery-side of the EV charger system. Accordingly, any short-circuit at the battery side can be removed quickly. Three software-based and hardware-based over-voltage protections (a total of six) are active at the front-end side, dc-link capacitor (C_{D}) and battery side (C_{B}). These three over-voltage protections shut down the whole system during any over-voltage phenomena that cause abnormal voltage variations at the front-end side, dc-link side or battery side.

An additional software-based phase-variation detector is used for the grid-side ac voltage. Using such fast and advanced protection, the phase-offset of the grid voltage is continuously compared with a phase reference, and during any short-circuit incident that may cause phase deviation on the front-end voltage, the fault is sensed in less than micro seconds and the system is shut down. This protection system operates faster than the above-mentioned over-current and over-voltage protections.

E. Designing the front-end inductors for both grid-connected and V2V operational modes

In the proposed EV charger, the front-end inductors L_{f1} and L_{f2} are shared by both the grid-connected and V2V operational modes. L_{f1} and L_{f2} are designed by considering the ripple factor (RF) of the front-end current i_{c} [17]. Since the grid-voltage is sinusoidal, the maximum inductor`s current ripple can be expressed by

$$\Delta I_{\mathrm{Lfpp}} = \frac{V_{\mathrm{D}} - v_{\mathrm{s,avg}}}{L_{\mathrm{f1}} + L_{\mathrm{f2}}} * DT_{\mathrm{s}} \qquad (7)$$

where V_{D} is the dc-link voltage, D is the duty cycle, T_{s} is the time period of a switching cycle, and $v_{\mathrm{s,avg}}$ is the fixed average output voltage of HB1. $v_{\mathrm{s,avg}}$ is equivalent to v_{s} in a switching cycle due to the chosen switching frequency f_{sw}, which is sufficiently higher than the line frequency f. When $D = m_{\mathrm{a}} \sin(\omega t)$, the maximum fluctuation of the inductor current is given by

$$\Delta I_{\mathrm{Lf1,max}}(\omega t) = \frac{V_{\mathrm{D}}T_{\mathrm{s}} - v_{\mathrm{s,avg}}}{2(L_{\mathrm{f1}} + L_{\mathrm{f2}})} * m_{\mathrm{a}} \sin(\omega t)(1 - m_{\mathrm{a}} \sin(\omega t)) \quad (8)$$

where m_{a} is the modulation index. If $m_{\mathrm{a}} = 1$, the inductor current becomes triangular so that the RMS value of the inductor current in one period can be obtained by

$$I_{\mathrm{Lf1,rms}} = \sqrt{\frac{2}{3\pi}\int_0^{\frac{\pi}{2}} \Delta I_{\mathrm{Lf1,max}}^2(\omega t) d(\omega t)} \quad (9)$$

which is $I_{\mathrm{Lf1,rms}} = \frac{\Delta I_{\mathrm{Lf1,max}}}{\sqrt{3}}$ after solving and simplifying. Then, substituting (8) into (9) results in

$$I_{\mathrm{Lf1,rms}} = \frac{V_{\mathrm{D}}T_{\mathrm{s}}}{4(L_{\mathrm{f1}} + L_{\mathrm{f2}})}\sqrt{\frac{2{m_{\mathrm{a}}}^2}{3\pi}\left[\frac{\pi}{4}\left(1 + \frac{3}{4}{m_{\mathrm{a}}}^2\right) - \frac{4}{3}m_{\mathrm{a}}\right]}. \quad (10)$$

The fundamental component of the inductor current is

$$I_{\mathrm{Lf1}} = \frac{V_{\mathrm{s}}}{Z} = m_{\mathrm{a}}\frac{V_{\mathrm{D}}T_{\mathrm{s,grid}}}{2\sqrt{2}\pi L_{\mathrm{b}}} \quad (11)$$

where V_{s} is the nominal value of the grid voltage and Z is the line impedance. L_{b}, which demonstrates the impedance of one period in an ac grid, is obtained by

$$L_{\mathrm{b}} = \frac{1}{2\pi f} * \frac{{V_{\mathrm{s,rms}}}^2}{P} \quad (12)$$

where P is the input power and $V_{\mathrm{s,rms}}$ is the RMS value of the grid voltage. Now, using (9), (10) and (11), the ripple factor (RF) can be calculated by

$$RF = \frac{I_{\mathrm{Lf1,rms}}}{I_{\mathrm{Lf1}}} = \frac{L_{\mathrm{b}}T_{\mathrm{s}}}{(L_{\mathrm{f1}} + L_{\mathrm{f2}})T_{\mathrm{s,grid}}}\sqrt{\frac{\pi}{3}\left[\frac{\pi}{4}\left(1 + \frac{3}{4}{m_{\mathrm{a}}}^2\right) - \frac{4}{3}m_{\mathrm{a}}\right]} \quad (13)$$

and from (13), the inductance value can be calculated as

$$L_{\mathrm{f1}} = L_{\mathrm{f2}} = \frac{1}{2}\frac{L_{\mathrm{b}}T_{\mathrm{s}}}{RF * T_{\mathrm{s,grid}}}\sqrt{\frac{\pi}{3}\left[\frac{\pi}{4}\left(1 + \frac{3}{4}{m_{\mathrm{a}}}^2\right) - \frac{4}{3}m_{\mathrm{a}}\right]}. \quad (14)$$

IV. PERFORMANCE EVALUATION OF THE EV CHARGER

Due to the lack of equipment in building the prototype of two EV chargers, the validity of the designed EV charger during the proposed V2V operation is evaluated using MATLAB/Simulink. The operation of the EV charger during the grid-connected mode is evaluated using the laboratory prototype of an EV charger. In this section, first, the proposed V2V operation [Function I] is evaluated, then the ability of the proposed EV charger to operate in the grid-connected mode by supporting the V2G, G2V, STATCOM and APF functions [Functions II, III and IV] is verified. The parameters summarized in Table I are used for both simulation and experimental implementation.

A. Performance evaluation during the proposed V2V operation

The aim of this section is to show the performance of the EV charger during the proposed V2V operation using simulation results. According to the design, during the V2V power transfer, V_{B} is set at 150 V, and the dc-link voltage V_{D} is regulated at 400 V. The front-end ac voltage v_{s} during the V2V operation is set to achieve 220 RMS voltage to be consistent with the value of the grid RMS voltage during the grid-connected operation. The control algorithm in Fig. 11 performs the voltage regulation while controlling the charging/discharging current.

Fig. 14 and Fig. 15 show the simulation results of the proposed V2V function through a case study in which two EVs are exchanging power through the V2V cable shown in Fig. 2. As shown in Fig. 14(a), the front-end voltage v_{s}, which is shared by the two EVs, is regulated using the control strategy of EVa presented in Fig. 11. As a result, the RMS of the front-end ac current i_{c} is increased to 15.2 A, showing the power flow of 3.34 kW between the two EVs. The dc-link voltage V_{D} in Fig. 14(b) is also regulated at 400 V. Fig. 14(c) and Fig. 14(d) show the battery voltage (V_{B}) of 151 V and the average battery current (I_{B}) of approximately 23.25 A corresponding to about 3.47 kW of power at the battery side of EVa. The state-of-charge (SOC) of EVa's battery is presented in Fig. 14(e), which indicates the discharging operation of EVa.

Fig. 15 shows the operation of EVb while receiving the charging power from EVa during the V2V operation. Fig. 15(a) shows the ac current i_{c} and the ac voltage v_{s}. Fig. 15(b) shows the dc-link voltage V_{D}, which is regulated at 400 V using the control system of EVb's converters. Fig. 15(c) and Fig. 15(d) show the battery voltage (V_{B}) of around 151 V and the battery current (I_{B}) of -20 A corresponding to about 3.02 kW of power received at the battery side of EVb. The HB2 in EVb uses a battery's current regulator; therefore, the current ripples are significantly lower than the current ripples of I_{B} in EVa. The V_{B} in EVb also exhibits lower ripples compared with V_{B} in EVa. This is because the lower double-frequency ripples (100 Hz) of V_{D} in EVb. In the simulation condition, the efficiency is calculated as 87% since the receiving power of EVb's battery is 3.02 kW and the sending power of EVa's battery is 3.47 kW.

The SOC of the battery is estimated using (15) as given by

$$SOC = 100 - \left(\frac{1}{Q_{\mathrm{B}}}\int_0^t i_{\mathrm{B}}(t)dt\right) \quad (15)$$

where $i_{\mathrm{B}}(t)$ is the instantaneous battery current and Q_{B} is the nominal capacity of the battery. Fig. 16(a) shows the voltage across the switch S_5. Fig. 16(b) shows the voltage across S_6. The inductor current of i_{L} is also shown in Fig. 16(c).

Fig. 17 presents a case study showing three discharging, standby and charging modes of EVa during the V2V operation. During the first time interval of $t = 0\ s$ to $t = 0.5\ s$, the power is transferred from EVa to EVb using the proposed V2V operation. As a result, as Fig. 17(a) shows, the battery of EVa discharges with 20 A current. This reduces the SOC of EVa's battery as shown in Fig. 17(c). Between $t = 0.5\ s$ to $t = 1\ s$, there is no power assigned by the control system. Therefore, as Figures 17(a) and 17(b) show, no current is transmitted between EVa and EVb. This results in a stable SOC on the batteries of both EVa and EVb as

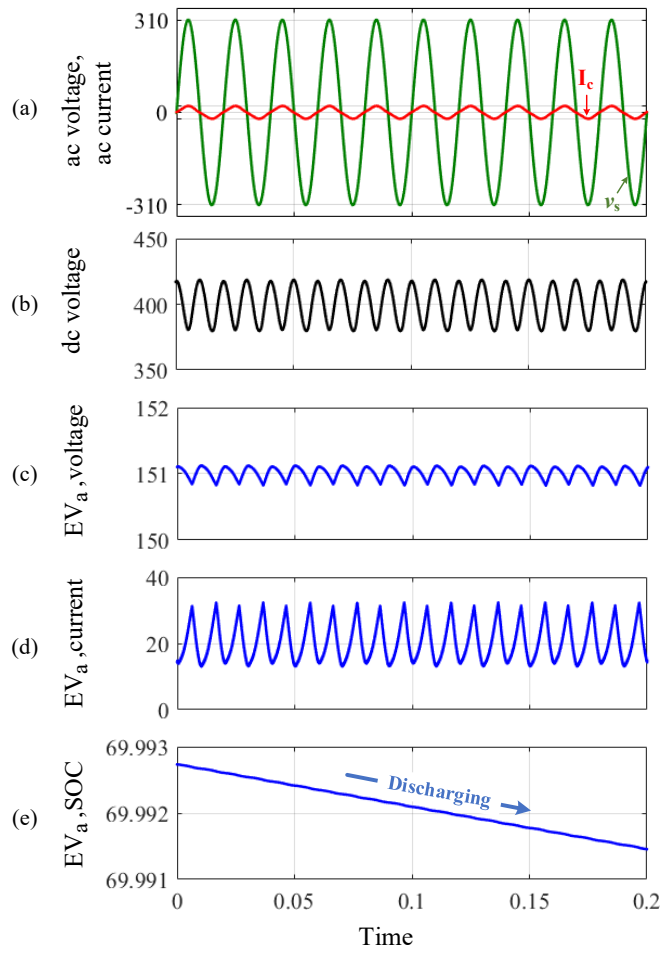

FIGURE 14. Simulation results of the proposed V2V operation [Function I]: a) EV_A`s front-end ac voltage V_s b) dc-link voltage V_D, c) dc-link voltage V_B, d) battery current I_B, e) SOC of the battery.

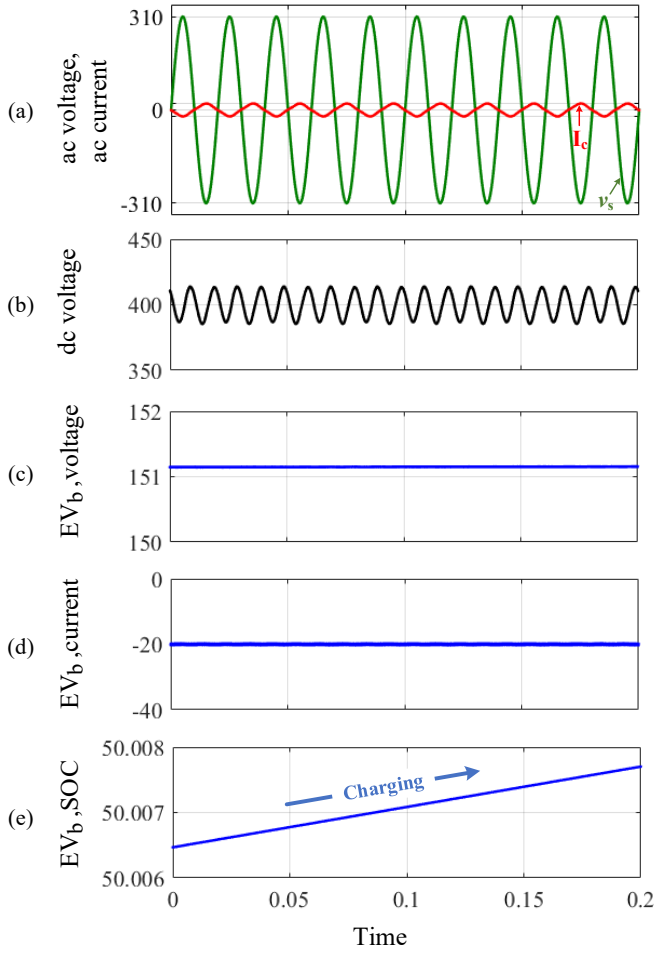

FIGURE 15. Simulation results of the proposed V2V operation [Function I]: a) EV_B`s front-end ac voltage V_s b) dc-link voltage V_D, c) dc-link voltage V_B, d) battery current I_B, e) SOC of the battery.

can be seen in Figures 17(c) and 17(d) for EVa. Between $t = 1\,s$ to $t = 1.5\,s$, the V2V operation is conducted via transferring power from EVb to EVa. Accordingly, the directions of currents and SOCs are reversed during this time interval.

B. Performance evaluation during the grid-connected mode

Fig. 18 shows the prototype of the EV charger. A SEMISTACK–IGBT is developed to implement HB1 and HB2 converters. The control systems presented in Fig. 11 and Fig. 12 are implemented on a TMS320F28335 DSP. A Sorensen XG 600-1.4 programmable dc power supply and a Chroma 63800 programmable load were employed to model a load, a V2V cable and the second EV unit. An MI 2883 EU Class S power-quality analyzer is also used for monitoring the power quality. This section evaluates the performance of the proposed EV charger to provide grid-connected functions such as Functions II, III and IV of the proposed EV charger.

Fig. 19 shows the experimental results of the EV charger's operation to support grid-connected functions. Figure 19(a) verifies the operation of the proposed EV charger to provide Functions II and III, which are V2G and the STATCOM

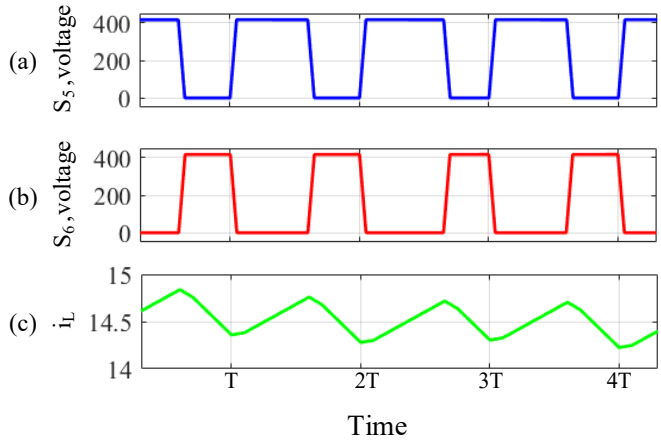

FIGURE 16. Simulation results of the proposed V2V operation [Function I]: a) voltage across S_5, b) voltages across S_6, c) inductor current I_L.

operation in inductive mode, respectively. In this test, the EV charger injects 165 W into the grid and circulates 150 VAR lagging. As shown, during this operation, the battery voltages V_B and V_D are maintained at 150 V and 220 V, respectively, which validate the steady-state stability of the control system shown in Fig. 12.

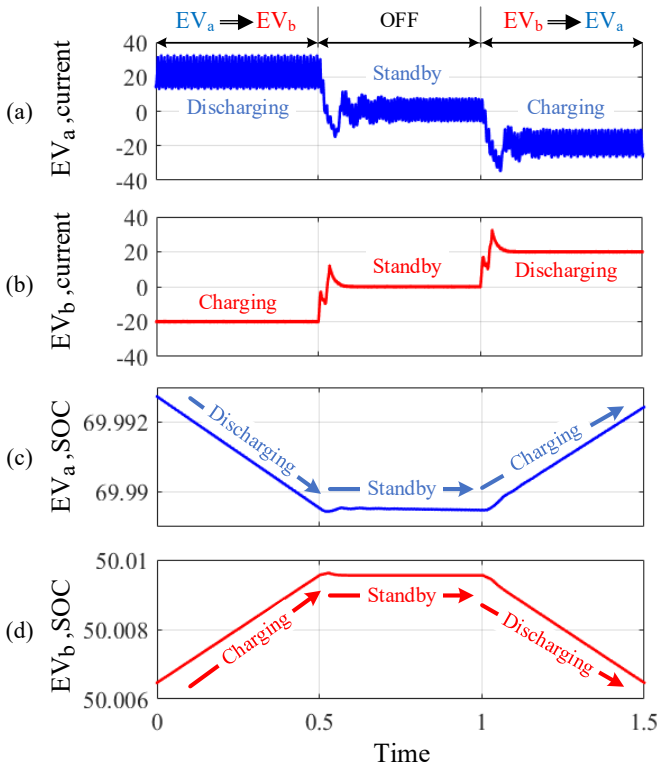

FIGURE 17. Simulation results of a case study when the direction of the transferring power is switched between EV_a and EV_b. A) battery current I_B of EV_a, b) battery current I_B of EV_b, c) SOC of EV_a, d) SOC of EV_b.

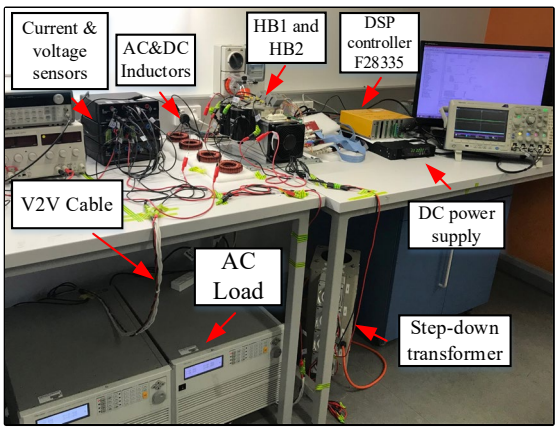

FIGURE 18. Experimental setup.

Fig. 19(b) shows the same test but in a capacitive mode. Fig. 20 shows the dynamic performance of the EV charger during several active and reactive power levels. Fig. 21 validates the performance of the multifunctional EV charger to supply Functions III and IV when the system works as a STATCOM for power-factor correction as well as an APF for harmonics reduction. For this test, the THD of the load current (i_L) is 25%, and the performance of the system is evaluated via comparing the source current i_s and i_L. Moreover, the power factor is set to 0.85, as shown by the phase shift between v_s and i_L. The reduced harmonics of i_s (3.37%) and its synchronization with the grid voltage v_s verifies that the EV charger can perfectly reduce the THD of i_s while it is also regulating the PF at almost unity.

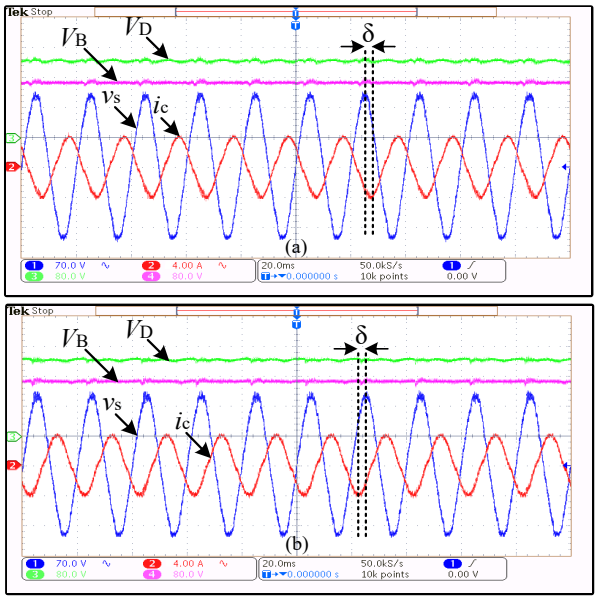

FIGURE 19. A) V2G and STATCOM operations [Functions II and III] during inductive mode P = 165 W, Q= 150 VAR lagging, and b) V2G and STATCOM operations during capacitive mode: P = 165 W, Q= 150 VAR leading. Front-end voltage v_s (70 V/div), converter current i_c (4 A/div), dc-link voltage V_D (80 V/div) and battery voltage V_B (80 V/div),

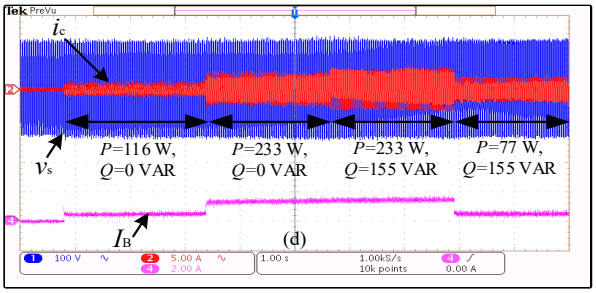

FIGURE 20. V2G and STATCOM operations [Functions II and III] during load switching, v_s (100 V/div), i_c (5 A/div) and I_B (2 A/div).

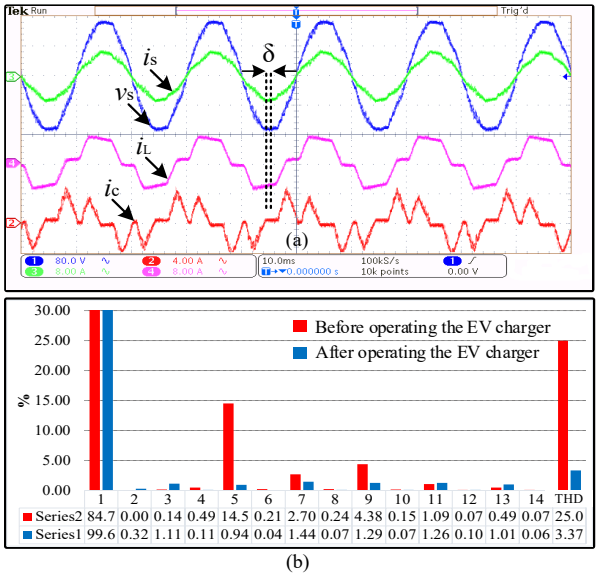

FIGURE 21. A) STATCOM and APF operation [Functions III and IV] when PF= 0.85 leading; EV charger supplies: $P \approx 0$ W, Q= 200 VAR, PF= 0.2 lagging, v_s (80 V/div), i_c (4 A/div), source current i_s (8 A/div) and load current i_L (8 A/div), b) THD of i_s before and after operating the EV charger.

TABLE III. Comparison of specifications of the proposed V2V and the portable charger

V2V technology	Input/output ports	Required extra charging infrastructure	Power ratio	Charging interface standard
Proposed V2V charging assistant	Input port: ac charging port of the first vehicle, which is an EV Output port: ac charging port of the second EV	A low-cost cable with two SAE J1772 connectors	Up to the EV charger's maximum power ratio	SAE J1772 for both input and output
Portable V2V charger in [28]	Input port: dc battery terminals of the first vehicle, which has an internal combustion engine Output port: ac charging port of the second EV	Two sets of connectors such as an input cable, an ac output cable with an SAE J1772 connector, an inverter along with its components such as switches, capacitors, inductors, the internal communication and control system, etc.	325 W	SAE J1772 only for output

Fig. 21(b) compares the harmonic spectrum and the THD of i_s before and after the EV charger`s operation measured by an MI 2883 EU Class S power analyzer. The THD (3.37%) is less than 5%, complying with the mandatory standard IEEE 1547.

V. CONCLUSION

This paper proposes a multifunctional EV charger with a novel V2V function that enables the charger to provide roadside charging assistance. As shown in Table III, unlike the V2V portable charger in [28], the proposed V2V does not require additional charging infrastructure. In addition, the proposed V2V operation meets the standard SAE J1772 and can be accomplished with the maximum power ratio of the EV charger. The V2V function enables an EV to be charged from another EV during an emergency when there is no access to a charging station. This function will become vital when the number of EVs grows and the demand for roadside charging assistance subsequently increases. The proposed EV charger is also able to supply the conventional main and ancillary functions such as V2G, G2V, reactive power support, and harmonics reduction. The design procedure of the proposed V2V function is analytically verified and validated through simulation in MATLAB/Simulink. The grid-connected functions are also tested and validated through experimental results. The future scope of this research is to build the prototype of a second EV charger so that the proposed V2V operation can be validated experimentally.

REFERENCES

[1] M. Yilmaz and P. T. Krein, "Review of battery charger topologies, charging power levels, and infrastructure for plug-in electric and hybrid vehicles," *IEEE transactions on Power Electronics,* vol. 28, pp. 2151-2169, 2013.

[2] S. Haghbin, S. Lundmark, M. Alakula, and O. Carlson, "Grid-connected integrated battery chargers in vehicle applications: Review and new solution," *IEEE Transactions on Industrial Electronics,* vol. 60, pp. 459-473, 2013.

[3] M. C. Kisacikoglu, B. Ozpineci, and L. M. Tolbert, "EV/PHEV bidirectional charger assessment for V2G reactive power operation," *IEEE Transactions on Power Electronics,* vol. 28, pp. 5717-5727, 2013.

[4] M. C. Kisacikoglu, M. Kesler, and L. M. Tolbert, "Single-phase on-board bidirectional PEV charger for V2G reactive power operation," *IEEE Transactions on Smart Grid,* vol. 6, pp. 767-775, 2015.

[5] M. Kesler, M. C. Kisacikoglu, and L. M. Tolbert, "Vehicle-to-grid reactive power operation using plug-in electric vehicle bidirectional offboard charger," *IEEE Transactions on Industrial Electronics,* vol. 61, pp. 6778-6784, 2014.

[6] C. Silvestre, D. M. Sousa, and A. Roque, "Reactive power compensation using on board stored energy in electric vehicles," in *IECON 2012-38th Annual Conference on IEEE Industrial Electronics Society*, 2012, pp. 5227-5232.

[7] L. Jia-zheng, Z. Yun, and L. Bo, "Application of Parallel Active Filter for the Electric Vehicle AC Charge Spots," in *Power and Energy Engineering Conference (APPEEC), 2012 Asia-Pacific*, 2012, pp. 1-4.

[8] M. C. Rodrigues, I. Souza, A. A. Ferreira, P. G. Barbosa, and H. A. Braga, "Integrated bidirectional single-phase vehicle-to-grid interface with active power filter capability," in *Power Electronics Conference (COBEP), 2013 Brazilian*, 2013, pp. 993-1000.

[9] M. C. Rodrigues, I. D. Souza, A. A. Ferreira, P. G. Barbosa, and H. A. Braga, "Simultaneous active power filter and G2V (or V2G) operation of EV on-board power electronics," in *Industrial Electronics Society, IECON 2013-39th Annual Conference of the IEEE*, 2013, pp. 4684-4689.

[10] M. Falahi, H.-M. Chou, M. Ehsani, L. Xie, and K. L. Butler-Purry, "Potential power quality benefits of electric vehicles," *IEEE Transactions on sustainable energy,* vol. 4, pp. 1016-1023, 2013.

[11] V. Monteiro, J. Pinto, and J. L. Afonso, "Operation modes for the electric vehicle in smart grids and smart homes: present and proposed modes," *IEEE Transactions on Vehicular Technology,* vol. 65, pp. 1007-1020, 2016.

[12] A. Boynuegri, M. Uzunoglu, O. Erdinç, and E. Gokalp, "A new perspective in grid connection of electric vehicles: Different operating modes for elimination of energy quality problems," *Applied Energy,* vol. 132, pp. 435-451, 2014.

[13] S. Taghizadeh, M. Hossain, J. Lu, and W. Water, "A unified multi-functional on-board EV charger for power-quality control in household networks," *Applied energy,* vol. 215, pp. 186-201, 2018.

[14] V. Monteiro, B. Exposto, J. Pinto, R. Almeida, J. C. Ferreira, A. A. N. Meléndez, *et al.*, "On-board electric vehicle battery charger with enhanced V2H operation mode," in *Industrial Electronics Society, IECON 2014-40th Annual Conference of the IEEE*, 2014, pp. 1636-1642.

[15] J. Pinto, V. Monteiro, H. Gonçalves, B. Exposto, D. Pedrosa, C. Couto, *et al.*, "Bidirectional battery charger with grid-to-vehicle, vehicle-to-grid and vehicle-to-home technologies," in *Industrial Electronics Society, IECON 2013-39th Annual Conference of the IEEE*, 2013, pp. 5934-5939.

[16] Y.-J. Lee, A. Khaligh, and A. Emadi, "Advanced integrated bidirectional AC/DC and DC/DC converter for plug-in hybrid electric vehicles," *IEEE Transactions on vehicular technology,* vol. 58, pp. 3970-3980, 2009.

[17] S. Kim and F.-S. Kang, "Multifunctional onboard battery charger for plug-in electric vehicles," *IEEE Transactions on Industrial Electronics,* vol. 62, pp. 3460-3472, 2015.
[18] I. IEC, "61851-1: Electric vehicle conductive charging system-part 1: General requirements,"" *IEC (International Electrotechnical Commission), Geneva, Switzerland,* 2010.
[19] S. Y. Kim, H.-S. Song, and K. Nam, "Idling port isolation control of three-port bidirectional converter for EVs," *IEEE Transactions on Power Electronics,* vol. 27, pp. 2495-2506, 2012.
[20] J. Pinto, V. Monteiro, H. Gonçalves, and J. L. Afonso, "Onboard reconfigurable battery charger for electric vehicles with traction-to-auxiliary mode," *IEEE Transactions on vehicular technology,* vol. 63, pp. 1104-1116, 2014.
[21] A.-M. Koufakis, E. S. Rigas, N. Bassiliades, and S. D. Ramchurn, "Towards an optimal EV charging scheduling scheme with V2G and V2V energy transfer," in *Smart Grid Communications (SmartGridComm), 2016 IEEE International Conference on*, 2016, pp. 302-307.
[22] P. You and Z. Yang, "Efficient optimal scheduling of charging station with multiple electric vehicles via v2v," in *Smart Grid Communications (SmartGridComm), 2014 IEEE International Conference on*, 2014, pp. 716-721.
[23] M. Wang, M. Ismail, R. Zhang, X. S. Shen, E. Serpedin, and K. Qaraqe, "A semi-distributed V2V fast charging strategy based on price control," in *Global Communications Conference (GLOBECOM), 2014 IEEE*, 2014, pp. 4550-4555.
[24] A. Mohamed, V. Salehi, T. Ma, and O. Mohammed, "Real-time energy management algorithm for plug-in hybrid electric vehicle charging parks involving sustainable energy," *IEEE Transactions on Sustainable Energy,* vol. 5, pp. 577-586, 2014.
[25] R. Zhang, X. Cheng, and L. Yang, "Flexible Energy Management Protocol for Cooperative EV-to-EV Charging," in *Global Communications Conference (GLOBECOM), 2016 IEEE*, 2016, pp. 1-6.
[26] D. Savio, V. Juliet, B. Chokkalingam, S. Padmanaban, and V. K. Ramachandaramurthy, "Design and Implementation of a Multiple Charging 2 Point Adapted Hybrid Microgrid Powered Electric 3 Vehicle Charging Station and Its Energy Management 4 Strategy 5," 2018.
[27] D. Jammer, "Real-time system and method for tracking, locating and recharging electric vehicles in transit," ed: Google Patents, 2017.
[28] J. E. P. ORTIZ and J. G. M. ELIZONDO, "Portable electric vehicle charging device," ed: Google Patents, 2018.
[29] R. Singh, S. Taghizadeh, N. M. L. Tan, and J. Pasupuleti, "Battery energy storage system for PV output power leveling," *Advances in Power Electronics,* vol. 2014, 2014.
[30] S. Rivera, S. Kouro, and B. Wu, "Charging Architectures for Electric and Plug-In Hybrid Electric Vehicles," in *Technologies and Applications for Smart Charging of Electric and Plug-in Hybrid Vehicles*, ed: Springer, 2017, pp. 111-149.
[31] A. Bidram, A. Davoudi, F. L. Lewis, and J. M. Guerrero, "Distributed cooperative secondary control of microgrids using feedback linearization," *IEEE Transactions on Power Systems,* vol. 28, pp. 3462-3470, 2013.
[32] N. L. Diaz, T. Dragičević, J. C. Vasquez, and J. M. Guerrero, "Intelligent distributed generation and storage units for DC microgrids—A new concept on cooperative control without communications beyond droop control," *IEEE Transactions on Smart Grid,* vol. 5, pp. 2476-2485, 2014.
[33] R. W. Erickson and D. Maksimovic, "Fundamentals of power electronics: Springer Science & Business Media," 2001.